

# Adaptive locally resonant metamaterials leveraging shape memory alloys

Vagner Candido de Sousa,<sup>1</sup> Christopher Sugino,<sup>2</sup> Carlos De Marqui Junior,<sup>1</sup>  
 and Alper Erturk<sup>2,a)</sup>

<sup>1</sup>Department of Aeronautical Engineering, Engineering School of São Carlos, University of São Paulo, São Carlos, SP 13566-590, Brazil

<sup>2</sup>G.W. Woodruff School of Mechanical Engineering, Georgia Institute of Technology, Atlanta, Georgia 30332, USA

(Received 29 March 2018; accepted 22 July 2018; published online 10 August 2018)

Locally resonant metamaterials leveraging shape memory alloy (SMA) springs are explored in this work in an effort to develop adaptive metamaterial configurations that can exhibit tunable bandgap properties as well as enhanced damping capabilities. An analytical model for a locally resonant metamaterial beam in transverse vibrations is combined with an SMA model for the resonator springs to investigate and leverage the potential of temperature-induced phase transformations and stress-induced hysteretic behavior of the springs. Two case studies are presented for this new class of smart metamaterials and the resulting finite metastructures. In one case, SMA resonators operate in the linear elastic regime, first at low temperature (martensitic behavior) and then at high temperature (austenitic behavior), demonstrating how the bandgap can be tuned to a different frequency range by altering the SMA elastic modulus with temperature. In the second case, the SMA springs are kept at high temperature at all times to operate in the nonlinear regime, so that the hysteresis associated with the SMA pseudoelastic effect is manifested, yielding additional dissipation over a range of frequencies, especially for the modes right outside the bandgap. *Published by AIP Publishing.*

<https://doi.org/10.1063/1.5031168>

## I. INTRODUCTION

Locally resonant metamaterials offer bandgap formation for wavelengths much longer than the lattice size, enabling low-frequency and wideband vibration attenuation.<sup>1–3</sup> The resonating elements of a locally resonant metamaterial can be mechanical<sup>1,4</sup> or electromechanical.<sup>5–7</sup> Researchers have proposed different implementations of resonators for elastic waves<sup>8–14</sup> and presented methods to predict the edge frequencies of the bandgap.<sup>2,3,15,16</sup> Some of the existing efforts include piezoelectrically coupled metamaterials and metastructures<sup>17–20</sup> as smart material-based concepts, including those leveraging ferroelectric phase transition.<sup>21</sup>

Acoustic/elastic metamaterials made from purely mechanical resonating components usually do not exhibit reconfigurable and adaptive characteristics since the bandgap frequency range (i.e., target frequency and bandwidth combination) is fixed for a given mass ratio and stiffness of the resonators. In this regard, the replacement of ordinary resonators by shape memory alloy (SMA) resonators can lead to an enhanced tunable metamaterial behavior. Among possible applications, SMAs can be exploited to decrease undesired frequency variations between resonators, which can decrease the bandgap width,<sup>3</sup> as well as to intentionally modify the behavior of specific resonators in order to design a metamaterial beam insensitive to multi-frequency excitations.<sup>22</sup>

The tuning of the bandgap is an attractive possibility since the elastic modulus of typical SMAs changes with temperature. For instance, the low-temperature modulus

(associated with a martensitic phase) can be around 30 GPa, while the high-temperature modulus (associated with an austenitic phase) can be as high as 70 GPa.<sup>23,24</sup> Assuming an SMA element in the absence of mechanical loading, the reversible transformation between these phases can be induced by varying the temperature by 30 °C to 40 °C in many SMAs. The temperatures for phase transformation are usually between –100 °C and 100 °C and depend mainly on the SMA composition, heat, and mechanical treatments.<sup>25–27</sup> For instance, typical nickel-titanium SMAs can exhibit phase transformation above room temperature for a larger titanium content, while nickel-rich SMAs can exhibit phase transformation below room temperature.<sup>25–27</sup> Therefore, it is possible to adjust the SMA modulus of elasticity by changing its temperature (e.g., through Joule heating<sup>28–30</sup>). As long as the SMA is not subjected to large deformations, it can be seen as a linear elastic spring with a variable-stiffness feature. For larger deformations, hysteretic behavior is associated with stress-induced martensitic phase transformation, providing additional damping capabilities.<sup>31–36</sup>

Although many different SMA models are available,<sup>24,37–41</sup> the models by Liang and Rogers<sup>31,42,43</sup> and Brinson<sup>23</sup> are among the most commonly employed and extended SMA models due to their simplicity and relatively good experimental agreement. The work of Liang and Rogers<sup>31,43</sup> presented the modeling of SMA helical springs based on classical spring design by employing the pure shear assumption and proposed the use of SMA springs in vibration problems. Brinson's work<sup>23</sup> proposed the separation of the martensite volume fraction (an internal variable defined to quantify the amount of phase transformation in the SMA) into a stress-induced part and a low-temperature part as well

<sup>a)</sup>Author to whom correspondence should be addressed: alper.erturk@me.gatech.edu

as a constitutive law accounting for non-constant material properties. Other efforts<sup>44–46</sup> further split the stress-induced martensite into tension and compression components in order to represent the asymmetric behavior usually observed in SMAs. Due to the attractive damping characteristics of SMAs,<sup>31–33</sup> the literature on the use of these materials in vibration attenuation and control problems includes seismic response enhancement and/or base isolation of structures,<sup>47–51</sup> adaptive vibration absorbers,<sup>52–54</sup> and beam-like (or plate-like) structures with embedded SMA members,<sup>55–57</sup> as well as beams or plates made of SMAs<sup>58–60</sup> and passive mitigation of aeroelastic oscillations,<sup>34–36</sup> among other applications.

In this work, we explore locally resonant metamaterials that exploit shape memory alloy springs toward developing adaptive metamaterials that exhibit tunable bandgap properties. An analytical model for a one-dimensional locally resonant metastructure (i.e., a metamaterial beam with specified boundary conditions) is combined with a shape memory spring model of the resonator springs to investigate and exploit the potential of temperature-induced phase transformations and stress-induced hysteretic behavior of the springs. Numerical case studies are presented for this new class of smart metamaterials and metastructures. First, the general aspects of a metamaterial beam with linear spring-mass resonators are briefly reviewed. Then, the linear springs of the resonators are modeled as SMA springs, and two different cases are presented. In the first case, the SMA springs operate in the linear elastic regime, first at low temperature (with martensitic elastic properties) and second at high temperature (with austenitic elastic properties), depicting how the bandgap can be tuned to a different frequency range by altering the SMA elastic modulus with temperature. In the other case, the SMA springs are kept at high temperature at all times and excited in the nonlinear regime, so that the hysteresis associated with the SMA pseudoelastic effect can be exploited (i.e., a stress-induced martensitic phase transformation followed by an austenitic phase transformation, yielding additional energy dissipation).

## II. THEORY

In order to investigate the behavior of a metamaterial beam with SMA-based resonators, a uniform Euler-Bernoulli

beam with fixed-free boundary conditions is considered for transverse vibrations. The coupled equations of motion are obtained for linear spring-mass resonators, following Sugino *et al.*<sup>2</sup> The equations are then modified to account for the effects of phase transformations in the SMAs (therefore replacing ordinary springs by SMA springs).

### A. Shape memory alloy model

Shape memory materials can recover their original (undeformed) shape multiple times by the application of external stimuli (such as heat) after undergoing a substantial deformation. The two most common effects of the SMAs are the shape memory effect and the pseudoelastic effect, defined in terms of the SMA temperature. In the shape memory effect, the SMA is deformed while at a relatively low temperature so that the original shape can be recovered only at a desired moment (later in time) by increasing the SMA temperature. In case the SMA is bearing a load, the SMA can act as an actuator. In the pseudoelastic effect, the SMA is kept at a relatively high temperature throughout the loading-unloading process such that the original shape is recovered when the mechanical loading is decreased. In such a case, the SMA behaves similar to a spring. Its spring behavior can be linear or nonlinear depending on the level of mechanical stress applied to the SMA.

The typical stress-strain behavior of an arbitrary SMA member tested at different temperatures is shown in Fig. 1(a). Although different temperatures are considered, a fully austenitic initial phase is assumed in all cases, and the lower temperatures are not low enough to yield a low-temperature martensitic phase transformation (so that only stress-induced martensitic phase transformation takes place). Note the unrecovered strain upon complete unloading at lower temperatures, the completely recovered strain upon unloading at higher temperatures, and the increase in the critical stress levels at which phase transformations take place with increasing temperature. Simplifying the discussion to the three SMA phases of more practical applications, the austenitic phase is the high-temperature phase, and the martensitic phase can be induced by either low temperature or by mechanical stress. Therefore, the transition between two

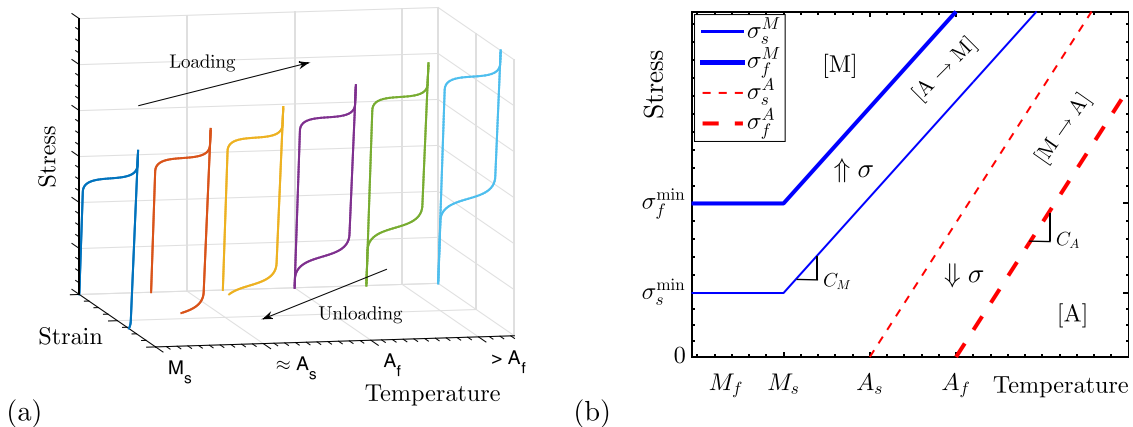


FIG. 1. (a) Typical SMA stress-strain behavior for different temperatures (assuming  $T > M_s$  and fully austenitic initial phase in all cases). (b) A simplified SMA phase transformation diagram. A and M stand for austenite and martensite, respectively.

SMA phases depends on a combination of temperature and mechanical stress. Based on experimental evidence, a phase diagram such as the one shown in Fig. 1(b) is widely employed to describe the required thermomechanical state of a given SMA for phase transformations to take place.<sup>23</sup>

Based on Fig. 1(b), the SMA critical stresses for phase transformation are given by<sup>23</sup>

$$\sigma_s^M = \sigma_s^{\min} + C_M(T - M_s) \text{ for } T > M_s, \text{ otherwise } \sigma_s^M = \sigma_s^{\min}, \quad (1)$$

$$\sigma_f^M = \sigma_f^{\min} + C_M(T - M_s) \text{ for } T > M_s, \text{ otherwise } \sigma_f^M = \sigma_f^{\min}, \quad (2)$$

$$\sigma_s^A = C_A(T - A_s) \text{ for } T \geq A_s, \quad (3)$$

$$\sigma_f^A = C_A(T - A_f) \text{ for } T \geq A_f, \quad (4)$$

where  $\sigma_s^M$  is the critical value of stress for the onset of stress-induced phase transformation (or forward transformation),  $\sigma_f^M$  is the critical stress for the completion of stress-induced transformation,  $\sigma_s^A$  is the stress value for the onset of the recovery of the austenitic phase (or reverse transformation), and  $\sigma_f^A$  is the stress value at which the austenitic phase is completely recovered. Additionally,  $\sigma_s^{\min}$  and  $\sigma_f^{\min}$  are minimum stresses at which stress-induced phase transformation begins and is completed, respectively;  $C_M$  and  $C_A$  represent the influence of temperature on critical stresses for forward and reverse transformations, respectively;  $M_s$  is the martensite start temperature,  $M_f$  is the martensite finish temperature,  $A_s$  is the austenite start temperature, and  $A_f$  is the austenite finish temperature (in the absence of stress), while  $T$  is the SMA temperature.<sup>23</sup>

Based on Ref. 23, the SMA martensitic fraction,  $\xi$ , can have a low-temperature part,  $\xi_T$ , and a stress-induced part,  $\xi_S$ , and can be defined as  $\xi = \xi_T + \xi_S$ . A stress-induced phase transformation takes place for  $\sigma_s^M < \sigma < \sigma_f^M$ . The corresponding martensitic fraction can be given by

$$\xi_S = \frac{1 - \xi_{S0}}{2} \cos\left(\pi \frac{\sigma - \sigma_f^M}{\sigma_s^{\min} - \sigma_f^{\min}}\right) + \frac{1 + \xi_{S0}}{2}, \quad (5)$$

where subscript 0 denotes an initial value (at the onset of the current phase transformation). In this case, the temperature-related part of the martensitic fraction can be given by

$$\xi_T = \xi_{T0} - \frac{\xi_{T0}}{1 - \xi_{S0}}(\xi_S - \xi_{S0}) + \Delta_T, \quad (6)$$

where

$$\Delta_T = \frac{1 - \xi_{T0}}{2} \left[ \cos\left(\pi \frac{T - M_f}{M_s - M_f}\right) + 1 \right], \quad (7)$$

if  $M_f < T < M_s$  and  $T < T_0$  (decreasing temperature), otherwise  $\Delta_T = 0$ .

During the reverse phase transformation (from martensite to austenite), the total martensitic fraction can be given by

$$\xi = \frac{\xi_0}{2} \left[ \cos\left(\pi \frac{T - A_s^\sigma}{A_f - A_s}\right) + 1 \right], \quad (8)$$

for  $T > A_s$  and  $\sigma_f^A < \sigma < \sigma_s^A$ , where  $A_s^\sigma = A_s + \sigma/C_A$  is the temperature at which the austenitic phase begins to stabilize with applied stress [see Fig. 1(b)]. The stress-induced and low-temperature components are, respectively,

$$\xi_S = \xi_{S0} - \frac{\xi_{S0}}{\xi_0}(\xi_0 - \xi), \quad (9)$$

$$\xi_T = \xi_{T0} - \frac{\xi_{T0}}{\xi_0}(\xi_0 - \xi). \quad (10)$$

The theory above can be applied along with classical spring design for the modeling of SMA helical springs.<sup>31,43</sup> The SMA spring force is represented by

$$f^{\text{sma}} = k(\xi)u(t) + Y(\xi), \quad (11)$$

where  $u(t)$  denotes the spring deflection. The martensitic-dependent SMA spring stiffness,  $k(\xi)$ , is represented by

$$k(\xi) = \frac{r^4}{4R^3N} G(\xi), \quad (12)$$

where  $r$  is the coil spring wire radius,  $R$  is the mean coil radius,  $N$  is the number of active coils, and  $G(\xi)$  is the martensite-dependent shear modulus. The shear modulus is expressed in terms of the martensitic fraction as

$$G(\xi) = G_A + \xi(G_M - G_A), \quad (13)$$

where  $G_M$  is the fully martensitic shear modulus and  $G_A$  is the fully austenitic shear modulus. It is assumed that the shear modulus ( $G$ ) and the elastic modulus ( $E$ ) are related to each other by  $E(\xi) = 2(1 + \nu)G(\xi)$ , where  $\nu$  is the Poisson's ratio.

The term  $Y(\xi)$  in Eq. (11) is related to the nonlinear stress-strain behavior of the SMA. It accounts for the changes in the SMA helical spring force when stress-induced phase transformations take place. By rearranging the SMA constitutive equation<sup>23,42</sup> and the SMA helical spring model,<sup>31,43</sup> this term becomes<sup>34</sup>

$$Y(\xi) = -\frac{\pi r^3}{2R} G(\xi) \epsilon_{\text{res}} \xi_S, \quad (14)$$

where  $\epsilon_{\text{res}}$  is the maximum recoverable strain of the SMA. It should be noted that this term depends on the stress-induced martensitic fraction (which does not include the low-temperature contribution to the total martensitic fraction). In the fully austenitic phase,  $\xi = 0$  and this term vanishes, and the SMA spring force is linear for austenitic elastic properties. In a fully stress-induced martensitic phase,  $\xi = \xi_S = 1$ . Upon a complete martensitic phase transformation, this term no longer changes so that further mechanical loading yields a linear force-displacement spring behavior for martensitic elastic properties. Moreover, for relatively small SMA deformations, no stress-induced phase transformation takes place so that  $\xi_S = 0$  and consequently  $Y(\xi) = 0$ . In such a case, the

force-displacement behavior of an SMA spring is linear, with spring constant given by Eq. (12), and the shear modulus changes only with the SMA temperature. Note, however, that for SMA helical springs, the stress-induced martensitic fraction never achieves unity since the core of the SMA cross-section is not expected to undergo large strains and stresses.

The mechanical constitutive equation for SMA wires under uniaxial loading<sup>23,42</sup> is extended for SMA bars under pure torsion<sup>31,43</sup> so that it can be employed to represent the hysteretic shear stress-strain behavior of SMA helical springs. By following the modelling approach of Refs. 31 and 43, the shear strain at the surface of an SMA spring can be estimated by a linear relation given by

$$\gamma = \frac{r}{2\pi R^2 N} u. \quad (15)$$

Equation (15) can be used with the linear shear stress-strain relationship given by  $\tau = G\gamma$ , where  $\tau$  is the shear stress, to verify if the corresponding shear stress is indeed in the linear elastic regime, or if it falls outside of the linear regime (therefore, within one of the transformation ranges). The phase transformation ranges were previously depicted in Fig. 1(b) and defined by Eqs. (1)–(4). In case the calculated value of shear stress is not in the linear regime, the actual value of the (nonlinear) shear stress is determined iteratively by employing the procedure described in Ref. 34. By employing such a procedure, the corresponding value of the martensitic fraction can also be determined.

The iterative procedure<sup>34</sup> is employed only during a phase transformation. In such a case, values for the shear stress within the transformation range (denoted by  $\tau_{\text{test}}$ ) are used in Eq. (5) or (8) (depending on the loading direction) along with the relation  $\sigma = \sqrt{3}\tau_{\text{test}}$ ,<sup>31,43</sup> yielding values for  $\xi$  between 0 and 1 (denoted by  $\xi_{\text{test}}$ ). Each pair ( $\xi_{\text{test}}$ ,  $\tau_{\text{test}}$ ) is verified in the following equation:

$$\tau_{\text{test}} - G(\xi)\gamma - G(\xi)\xi_{\text{test}}\varepsilon_{\text{res}} = 0, \quad (16)$$

along with the shear strain given by Eq. (15) and the current value of the shear modulus to determine the stress level and martensitic fraction corresponding to given spring deflection and temperature. Equation (16) is based on the constitutive relationship for SMAs with non-constant material functions of Ref. 23 (modified by the pure shear assumption<sup>31,43</sup>) and is presented with more details in Ref. 34. In this way, the shear modulus [Eq. (13)], the spring stiffness [Eq. (12)], and therefore the nonlinear spring force [Eq. (11)] can be updated according to the current level of phase transformation.

## B. Locally resonant metamaterial beam model

Consider a cantilevered Euler-Bernoulli beam with bending stiffness  $EI$ , mass per unit length  $m$ , and length  $L$ . The beam is assumed to be undamped (without loss of generality) since modal damping can be introduced later. The oscillatory base displacement applied to the beam in the transverse direction is  $w_b(t)$ , while the relative transverse displacement is  $w(x, t)$ , such that the absolute displacement is

$w_{\text{abs}}(x, t) = w_b(t) + w(x, t)$ . We assume that there are  $S$  undamped resonators attached to the beam, as shown in Fig. 2, at locations  $x_j$ , with masses  $m_j$ , and relative displacements  $u_j$ , for  $j = 1 \dots S$ . For derivation of the equations of motion, consider linear resonators with stiffness  $k_j$  and natural frequencies  $\omega_{a,j}^2 = k_j/m_j$ . The final equations of motion (for linear resonators) will be modified later for the case of SMA resonators.

The governing equation for the beam in physical coordinates is<sup>2</sup>

$$EI \frac{\partial^4 w}{\partial x^4} + m \frac{\partial^2 w}{\partial t^2} - \sum_{j=1}^S m_j \omega_{a,j}^2 u_j(t) \delta(x - x_j) = -m \ddot{w}_b(t), \quad (17)$$

where  $\delta(x)$  is the Dirac delta function. The governing equation for each resonator is

$$\ddot{u}_j(t) + \omega_{a,j}^2 u_j(t) + \frac{\partial^2 w}{\partial t^2}(x_j, t) = -\ddot{w}_b(t). \quad (18)$$

Assume that the natural frequencies  $\omega_i$  and mode shapes  $\phi_i(x)$  of the plain beam (without the resonators) are known<sup>61</sup> and that the mode shapes are normalized such that

$$\int_0^L \phi_i(x) \phi_j(x) dx = L \delta_{ij}, \quad (19)$$

where  $\delta_{ij}$  is the Kronecker delta.

Using an assumed-modes expansion with  $N$  terms and employing the corresponding plain beam mode shapes as basis functions, we assume

$$w(x, t) = \sum_{i=1}^N \phi_i(x) \eta_i(t). \quad (20)$$

Substituting Eq. (20) into Eqs. (17) and (18), applying orthogonality conditions,<sup>61</sup> and rearranging provide the governing equations in modal coordinates.<sup>2</sup> Using the expression for the SMA spring behavior, Eq. (11), the governing equations become

$$\sum_{i=1}^N \left[ \delta_{ik} + \sum_{j=1}^S \hat{m}_j \phi_i(x_j) \phi_k(x_j) \right] \ddot{\eta}_i(t) + \sum_{j=1}^S \hat{m}_j \phi_k(x_j) \ddot{u}_j(t) + \omega_k^2 \eta_k(t) = -\ddot{w}_b(t) \left( \int_0^L \phi_k(x) dx + \sum_{j=1}^S \hat{m}_j \phi_k(x_j) \right), \quad (21)$$

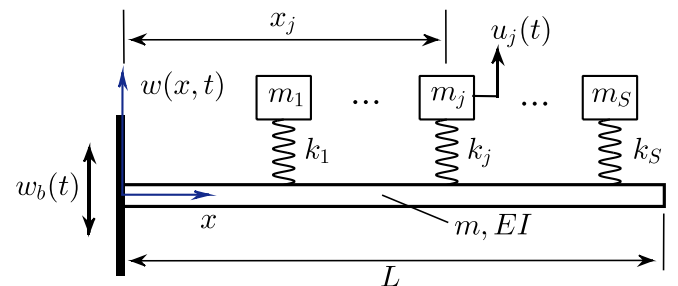


FIG. 2. Schematic of a locally resonant metamaterial beam (cantilever with spring-mass resonators) under transverse base excitation.

$$\ddot{u}_j(t) + \omega(\xi)_{a,j}^2 u_j(t) + \bar{Y}_j(\xi) + \sum_{i=1}^N \ddot{\eta}_i(t) \phi_i(x_j) = -\ddot{w}_b(t), \quad (22)$$

where  $\hat{m}_j = m_j/(mL)$  is the  $j$ th normalized resonator mass,  $\omega(\xi)_{a,j}^2 = k(\xi_j)/m_j$  is the squared natural frequency of the  $j$ th SMA resonator, in which  $k(\xi_j)$  is given by Eq. (12), and  $\bar{Y}_j(\xi) = Y(\xi_j)/m_j$ , in which  $Y(\xi)$  is given by Eq. (14). Note that for linear resonators  $\omega_{a,j}$  is constant (since  $k_j$  is fixed) and  $Y(\xi) = 0$ . Furthermore, in the SMA case, the martensitic fraction ( $\xi$ ) can have contributions of both low-temperature and stress-induced parts,<sup>23</sup> or contribution of only one of these variants, depending on the problem under consideration (stiffness variation or hysteresis). The free indices  $k$  and  $j$  go from 1 to  $N$  and 1 to  $S$ , respectively, therefore forming a system of  $N + S$  coupled second-order ordinary differential equations. The index  $i$  denotes the coupling between modes and goes from 1 to  $N$ .

Based on the theory in Ref. 2, the new resonance frequency branches are

$$\hat{\omega}^+ = \sqrt{\frac{1 + \mu + \Omega_k^2}{2} \left( 1 + \sqrt{1 - \frac{4\Omega_k^2}{(1 + \mu + \Omega_k^2)^2}} \right)}, \quad (23)$$

$$\hat{\omega}^- = \sqrt{\frac{1 + \mu + \Omega_k^2}{2} \left( 1 - \sqrt{1 - \frac{4\Omega_k^2}{(1 + \mu + \Omega_k^2)^2}} \right)}, \quad (24)$$

where  $\hat{\omega} = \omega/\omega_t$  and  $\Omega_k = \omega_k/\omega_t$  are the excitation frequency and the plain beam natural frequencies normalized by the target frequency, respectively. Superscripts  $+$  and  $-$  denote the higher and lower resonances, respectively. Moreover,  $\mu$  is the ratio of the total mass of the resonators to the plain beam mass.<sup>2</sup> By analyzing the limiting values of these frequencies, the new resonances of each mode cannot be in the range

$$\omega_t < \omega < \omega_t \sqrt{1 + \mu}, \quad (25)$$

which defines the limits of the bandgap. The bandwidth of the bandgap is then

$$\Delta\omega = \omega_t \left( \sqrt{1 + \mu} - 1 \right). \quad (26)$$

As usual in the SMA literature, no distinction between the low-temperature martensite and the stress-induced martensite is made here with regard to the modulus of elasticity (the modulus changes only between the martensitic and austenitic phases). Assume that the SMA modulus,  $E(\xi)$ , is bounded within  $E_M$  and  $E_A$ , that  $E_A$  is two to three times greater than  $E_M$  (as commonly reported for many SMAs), and also that the transition between these values is a linear function of the martensitic volume fraction  $\xi$ . When the SMA is in a fully martensitic phase (induced either by low temperature or mechanical stress),  $\xi = 1$  and hence  $E(\xi) = E_M$ . In the fully austenitic phase (induced by high temperature),  $\xi = 0$  and

$E(\xi) = E_A$ . For any mix of austenitic and martensitic phases,  $0 < \xi < 1$  and  $E_M < E(\xi) < E_A$ . The stiffness of the SMA resonators is, therefore, in the range  $k_j^M \leq k_j(\xi) \leq k_j^A$ .

Considering that the elastic modulus of the SMAs can change with the martensitic fraction, the target frequency  $\omega_t(\xi)$  of the metamaterial with SMA resonators (where  $\omega_t(\xi) = \omega(\xi)_{a,j}$  in this work) is bounded within  $\omega_t^M = \sqrt{k_j^M/m_j}$  (for the fully martensitic phase) and  $\omega_t^A = \sqrt{k_j^A/m_j}$  (for the fully austenitic phase). Since the bandgap width [Eq. (26)] changes with the resonator natural frequency, the bandgap width of a metamaterial beam with SMA resonators is bounded within  $\Delta\omega^M = \omega_t^M (\sqrt{1 + \mu} - 1)$  and  $\Delta\omega^A = \omega_t^A (\sqrt{1 + \mu} - 1)$  as the SMAs change from the fully martensitic phase to the fully austenitic phase, respectively. Note that the target frequency and the bandgap width change according to the martensitic fraction of the SMAs (adjusted by temperature), while the mass ratio is not modified. For a constant mass ratio  $\mu$ , the ratio  $\Delta\omega/\omega_t$  is the same in all cases. For convenience, we can express the austenitic modulus in terms of the martensitic modulus (i.e.,  $E_A = \alpha E_M$ ) in the equations above. It follows that  $\Delta\omega^A/\Delta\omega^M = \sqrt{E_A/E_M}$  is the increase in the bandgap width achieved for the SMA under consideration when it changes from the martensitic phase to the austenitic phase. This relationship provides a good insight based just on the elastic properties of the SMA at hand, without any assumptions for the geometry of the SMA members.

### III. CASE STUDIES AND RESULTS

Equations (21) and (22) are solved in the time domain in this work by using a Runge-Kutta method to accommodate the SMA model. For simulation purposes, four modes were considered (with the understanding that a greater number can be required to capture specific behaviors which are not of concern in this work). Five resonators were assumed since this is the number of resonators of the experimental validation presented in Ref. 2. Damping was also introduced to capture the finite resonant amplitudes.<sup>2</sup>

#### A. Metamaterial beam with passive linear resonators

This section briefly reviews the metamaterial beam with linear resonators. The resonator frequencies are chosen to have the bandgap centered at the second natural frequency of the plain beam. Figure 3(a) shows a transmissibility plot for the free end of the beam. Frequency responses for both the plain beam (without the resonators) and the metamaterial beam (with linear resonators) are shown, as a validation of the time-domain numerical solution scheme against the results in Sugino *et al.*<sup>2</sup> One can see Ref. 2 for experimental validations of the purely linear and passive theory. Time responses are shown in Fig. 3(b) for different values of excitation frequency (normalized by the first natural frequency of the plain beam).

#### B. Metamaterial beam with shape memory resonators

In the following, linear resonators will be replaced by SMA resonators. First, the variation of the SMA elastic

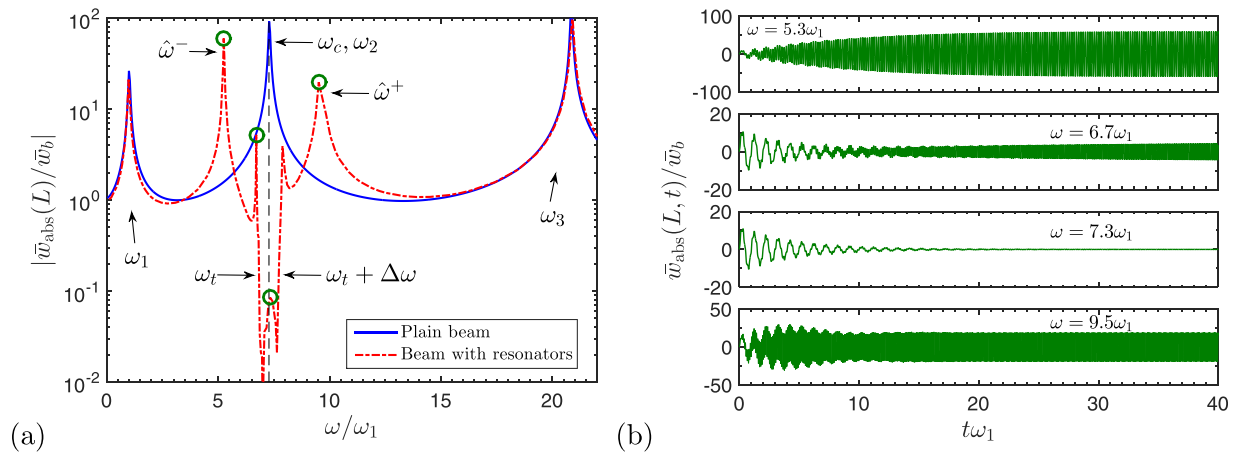


FIG. 3. (a) Transmissibility plots for the free end of the beam. The transmissibility for the plain beam (without the resonators) is shown in blue (solid line). The transmissibility for the metamaterial beam (with linear resonators) is shown in red (dashed line). The bandgap is centered at the second natural frequency of the plain beam. (b) Representative time responses for the free end of the metamaterial beam with linear resonators at different excitation frequencies. The frequencies in (b) correspond to the markers in (a), namely, the  $\omega/\omega_1$  ratios of 5.3, 6.7, 7.3, and 9.5.

modulus with temperature is considered for tuning. After that, the hysteresis associated with the SMA pseudoelastic effect is exploited. The martensitic and the austenitic moduli assumed for the simulations are  $E_M = 35$  GPa and  $E_A = 70$  GPa, respectively. The assumed values for the minimum stresses for the onset and completion of stress-induced phase transformations are  $\sigma_s^{\min} = 20$  MPa and  $\sigma_f^{\min} = 80$  MPa, respectively. The stress-temperature slopes (as depicted in Fig. 1) are assumed as  $C_M = 4$  MPa  $^{\circ}\text{C}^{-1}$  and  $C_A = 6$  MPa  $^{\circ}\text{C}^{-1}$ . The actual critical stresses are given by Eqs. (1)–(4) for a given SMA temperature, while the temperature depends on the case study. The maximum recoverable strain of the SMA is assumed as  $\varepsilon_L = 0.067$ . The assumed Poisson's ratio (to estimate the shear modulus) is  $\nu = 0.33$ . The SMA transition temperatures assumed for the simulations are  $M_f = 29$   $^{\circ}\text{C}$ ,  $M_s = 42$   $^{\circ}\text{C}$ ,  $A_s = 43$   $^{\circ}\text{C}$ , and  $A_f = 58$   $^{\circ}\text{C}$  (also employed in Ref. 34). The geometry of the SMA springs can be calculated using the equations presented in Sec. II A according to the metamaterial being considered. For the particular cases of this work, SMA springs with 0.95 mm wire diameter and 8 mm mean coil diameter are assumed (the same as Ref. 34). The number of coils is calculated [using Eq. (12)] according to a prescribed value of target frequency (and known resonator mass), yielding the required stiffness of the resonators.

### 1. Leveraging temperature-induced phase transformations

In this section, the reversible change in the elastic modulus of an SMA (and the corresponding change in the resonator stiffness) by properly adjusting its temperature is exploited to enable the tuning of the metamaterial target frequency, forming the basis of an adaptive metamaterial beam. The discussion is limited to cases in which the SMA members operate in the linear elastic regime (the deformation achieved by the SMA is not large enough to result in a stress-induced phase transformation). Note that, although the shape memory effect is not leveraged in the sense of shape recovery in this work (e.g., by heating an SMA that was substantially deformed while at a relatively low temperature),

the reversible transition between the martensitic phase and the austenitic phase (related to the shape memory effect) will be exploited.

Figure 4 gives some insight into the characteristics of the bandgap [using Eqs. (23) and (24)]. The behavior depicted in Fig. 4(a) was previously discussed in Ref. 2 for a metastructure with linear resonators and is briefly recalled here since it will be affected by the phase transformation of the SMA resonators. Figure 4(a) depicts two arbitrary cases, for the unity mass ratio and a lower mass ratio ( $\mu = 1.0$  and  $\mu = 0.3$ , respectively). The mass ratio  $\mu = 0.3$  is also considered in the cases of Fig. 4(b) (and in all cases that will be presented next in this work), depicting how the new resonances can change depending on the current value of the SMA modulus. It is noteworthy in Fig. 4(b) that the new higher resonances are closer to the upper bound of the bandgap when the target frequency increases from  $\omega_t^M$  to  $\omega_t^A$  as the SMAs change from fully martensite to fully austenite. In this particular case, the elastic moduli of the SMA resonators,  $E(\xi)$ , change from  $E_M = 35$  GPa to  $E_A = 70$  GPa when the SMA steady-state temperature,  $T$ , changes from  $M_f = 29$   $^{\circ}\text{C}$  to  $A_f = 58$   $^{\circ}\text{C}$ . Since the  $M_f$  temperature is slightly above room temperature, the SMA cooling (yielding the martensitic phase) can be achieved simply by natural convection in the absence of the heat source.

Figure 5(a) shows the transmissibility (tip displacement to base displacement ratio) of the metamaterial beam with SMA resonators. Two distinct limiting cases are shown. The bandgap in a lower frequency range is obtained for the SMAs at low temperature (in a fully martensitic phase). The bandgap in a higher frequency range is obtained for the SMAs at high temperature (in the fully austenitic phase). Figure 5(b) shows the bandgap that would be achieved by properly varying the temperature of the SMAs. Typical SMA properties are assumed (especially the fully martensitic and fully austenitic elastic moduli, which are the most influential parameters of this case) so that the behavior depicted in Fig. 5 is realistic for experimental implementation. In an experimental setup, the range of temperature can be achieved by

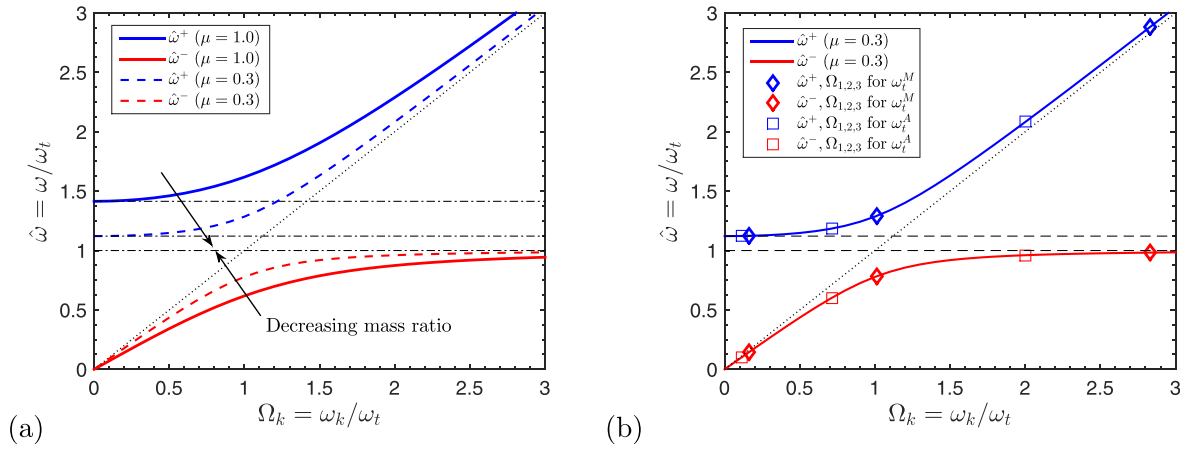


FIG. 4. Resonant frequencies of the representative metastructure (a) for linear resonators and mass ratios of unity and 0.3 and (b) for SMA resonators with a mass ratio of 0.3, at both fully martensitic and fully austenitic phases.

Joule heating or heat exchange with the environment, for example. Joule heating using DC power supplies is commonly reported in the literature when SMA wires are considered (in straight or coiled forms). Joule heating can also be achieved using eddy currents associated with electromagnetic induction. The latter (induction heating) is recommended for bulk SMAs, such as SMA beams or plates.<sup>30</sup>

Note that, in the particular case of Fig. 5, it is assumed that the SMAs do not undergo stress-induced phase transformation, so that the changes in the martensitic fraction are only due to the changes in the temperature of the SMAs. It is also assumed that the temperatures of all SMA springs are the same (steady-state temperature is assumed). To clarify the hypothesis of linear behavior (with changes only in the slope of the stress-strain behavior depending on the temperature of the SMAs), the SMA model described in Sec. II A is used to determine the stress values corresponding to the spring deflections of the SMA resonators (which are required to be smaller than the critical value depicted in Fig. 1 and given by Eq. (1) for the SMA properties presented earlier in this work). Considering this case of tuning of the metamaterial by temperature change, an attractive set of SMA properties can be given by large separation between the martensitic

and austenitic moduli (yielding larger tunability of the bandgap) associated with a narrow thermal hysteresis (therefore requiring lower input heat to achieve the “high-temperature” state of the austenitic phase).

## 2. Leveraging the pseudoelastic effect at a fixed temperature

The pseudoelastic effect of SMAs is exploited in this section. A fundamental difference is that the martensitic phase is only induced by high enough mechanical stress and not by low temperature. In the pseudoelastic effect, the SMA springs behave like ordinary, linear-elastic springs at relatively small deformation. In such a case, the SMA spring behavior can be associated with the mechanical properties of the austenitic phase. At larger deformations, stress-induced phase transformation (from austenite to martensite) can take place. The larger the mechanical loading, the larger the amount of phase transformation. However, as a circular bar under torsion, the SMA spring will never experience high enough stress levels at its core to completely transform into martensite (along the radius of the SMA wire). Considering physically achievable deformations (which do not exceed the

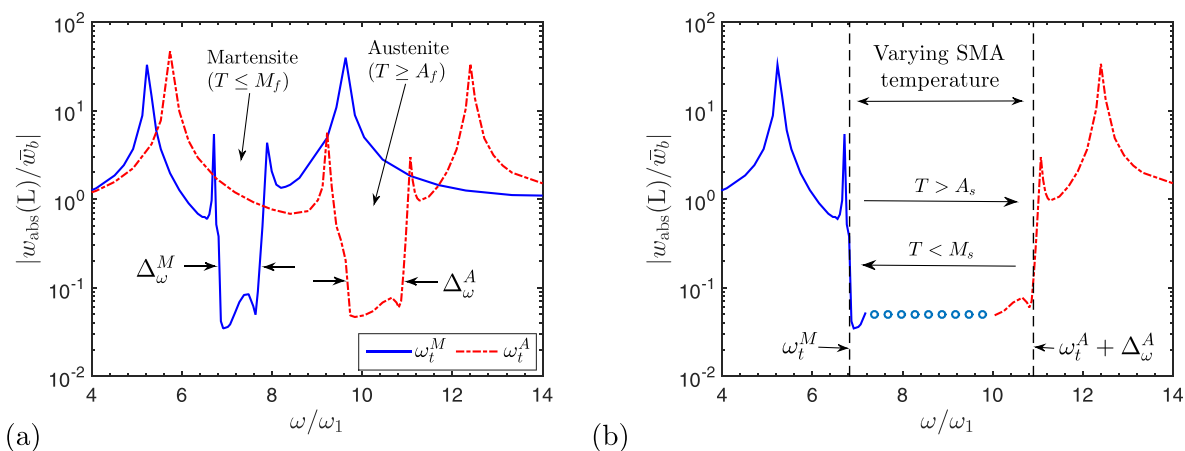


FIG. 5. Transmissibility graphs for a metamaterial beam with SMA resonators: (a) Two distinct limiting cases for the SMAs at low temperature (bandgap at a lower frequency range) and at high temperature (bandgap at a higher frequency range). (b) Bandgap that can be obtained by properly varying the temperature of the SMAs in an adaptive way.

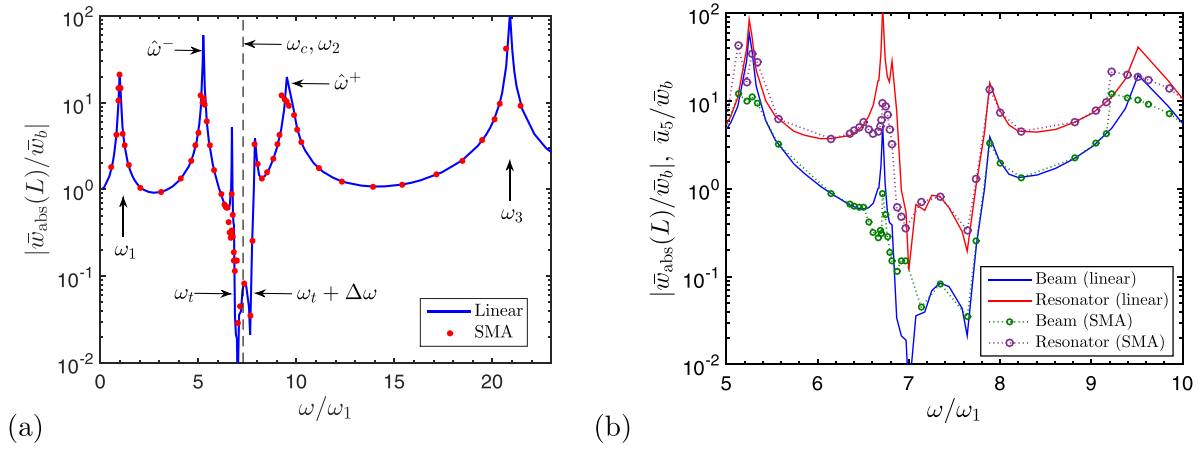


FIG. 6. (a) Transmissibility plot for the free end of a metamaterial beam with SMA resonators in the pseudoelastic regime. (b) Close-up for the bandgap region, including the normalized displacement of the resonator located at the free end of the beam. The case with linear resonators is also shown.

recoverable limits of the SMA), the SMA spring behavior during phase transformation can be associated with arbitrary mechanical properties (bounded by the fully martensitic and fully austenitic elastic properties). The austenitic phase can be recovered, while the SMA is mechanically unloaded due to its high-temperature state.

The pseudoelastic effect requires  $T \geq A_f$ . The particular case of  $T = A_f$  is assumed, so that the SMAs are in the fully austenitic phase in the absence of mechanical loading. The SMA critical stresses are based on the phase diagram of Fig. 1 along with Eqs. (1)–(4). As previously shown for a metamaterial beam with linear resonators (Fig. 3), Fig. 6 shows the transmissibility for the metamaterial beam with SMA resonators operating in the pseudoelastic regime. Figure 6(a) displays the transmissibility for the excitation frequency up to slightly above the third natural frequency of the beam. Figure 6(b) shows a closer view of the bandgap region and includes the normalized displacement of the resonator

located at the free end of the beam. The resonances associated with the two new resonant frequencies, the lower bound of the bandgap and the third natural frequency of the plain beam, exhibit a moderate attenuation. At those particular excitation frequencies, the resonators undergo larger displacements so that the achieved stress levels are high enough to induce some amount of martensitic phase transformation (yielding some hysteretic dissipation). One can also note a softening behavior at those resonances related to the increase in the martensitic fraction in the SMAs, which decrease their elastic moduli during the loading stage. The austenitic phase and therefore the fully austenitic elastic modulus are recovered during the unloading stage of the SMAs.

For the case of a metamaterial beam with SMA resonators [repeated in Fig. 7(a)], representative time responses are shown in Fig. 7(b) for different values of the excitation frequency. The corresponding martensitic fraction of the SMA resonators is shown in Fig. 7(c). Each of the SMA resonators

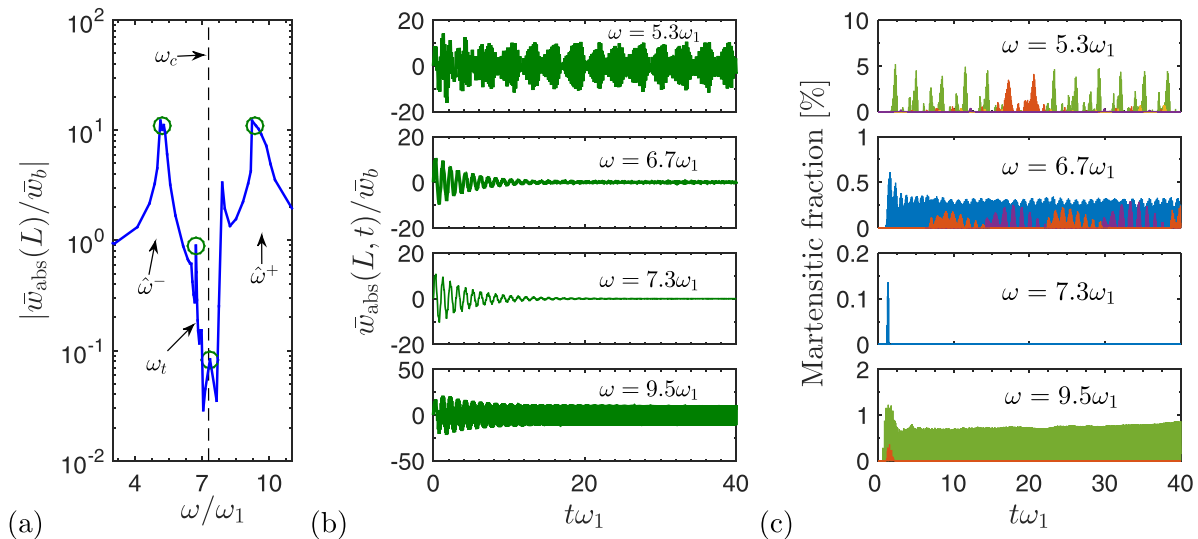


FIG. 7. (a) Transmissibility plot for the case with SMA resonators. (b) Representative time responses for the free end of the metamaterial beam with SMA resonators (at different excitation frequencies). (c) Martensitic fraction of the SMA resonators. The SMA resonators are represented in blue, red, yellow, purple, and green (from the closest to the clamped end of the main beam to the one located at the free end of the main beam, respectively). Not all SMA resonators exhibit phase transformation at a given excitation frequency so that some of them are omitted. The frequencies in (b) and (c) correspond to the markers in (a), namely, the  $\omega/\omega_1$  ratios of 5.3, 6.7, 7.3, and 9.5.

is represented by a different color (details in the caption of the figure) to highlight that not all of them exhibit some amount of martensitic fraction at a given excitation frequency. A significant attenuation is predicted for  $\omega/\omega_1 = 5.3$  [cf. Fig. 6(a)], where two SMA resonators (in green and red) undergo significant phase transformation and therefore achieving larger levels of hysteretic damping. There is also a less significant contribution of two other SMA resonators (in yellow and purple). For  $\omega/\omega_1 = 6.7$ , although three SMA resonators exhibit phase transformation, the achieved amount of martensitic

fraction (hence hysteresis) is minor since the transmissibility was originally smaller than that for  $\omega/\omega_1 = 5.3$ . The same applies for  $\omega/\omega_1 = 9.5$ . At  $\omega/\omega_1 = 7.3$ , there is no significant phase transformation in any of the SMA resonators so that the predicted behavior is similar to that of Fig. 6(a) for linear resonators.

In order to gain more insight into the behavior of the metamaterial beam (and resonators), Fig. 8 shows the transverse displacement of the beam with SMA resonators for the resonances of Fig. 6 (cases for linear resonators are included).

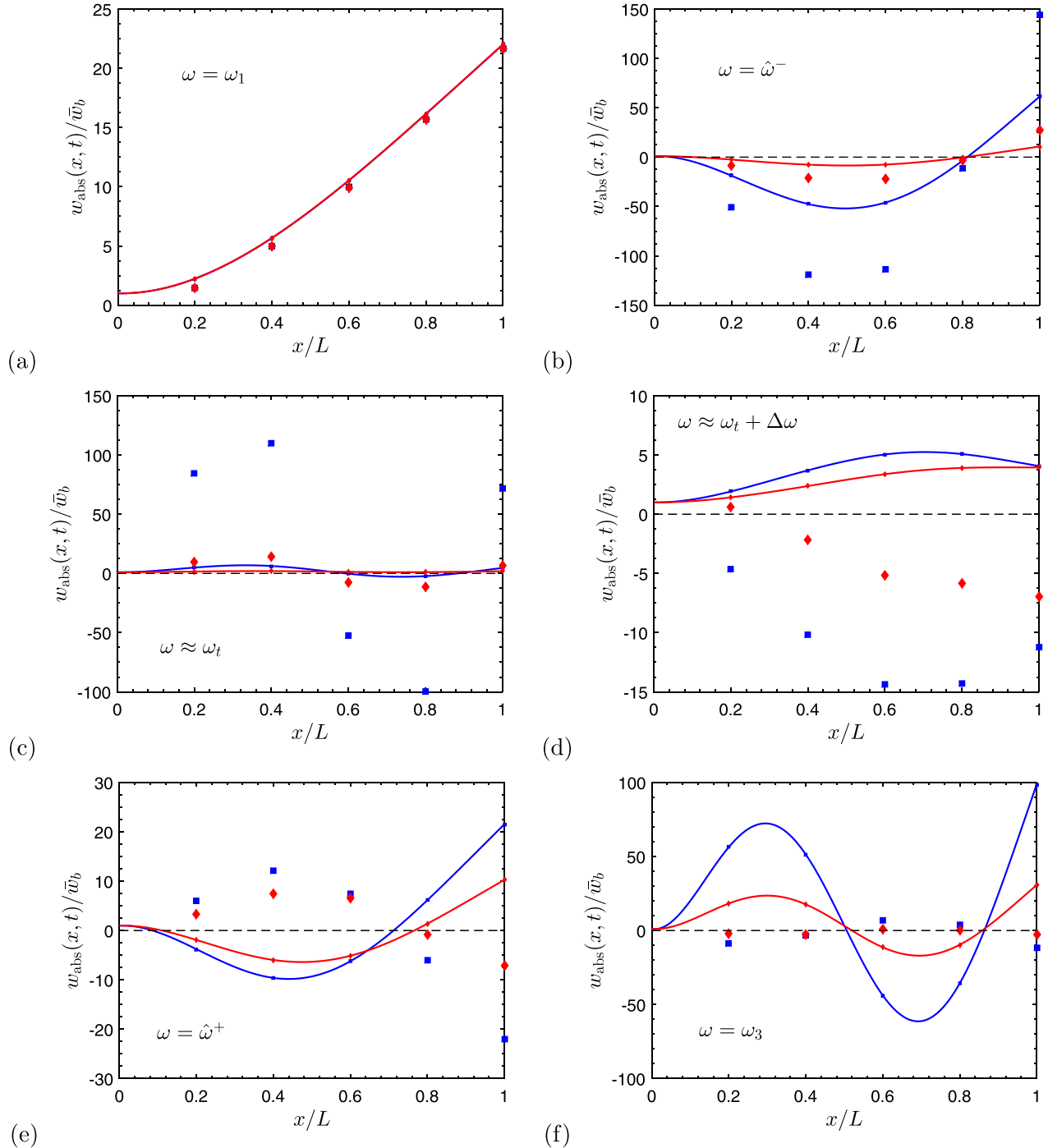


FIG. 8. Transverse displacements of the metamaterial beam with SMA resonators (in red, with diamond markers for the resonators) and of the metamaterial beam with purely mechanical linear resonators (in blue, with square markers for the resonators) at the resonance frequencies seen in Fig. 6 [increasing frequency from (a) to (f)].

The displacement is shown along the beam length for time instants corresponding to peak displacements at the free end of the beam in the forced response. The beam and the resonators are in phase for excitation frequencies up to the target frequency and out-of-phase higher frequencies. The improvements (in terms of attenuation) are related to the pseudoelastic hysteresis of the SMAs, achieved when the displacements of the resonators are large enough to induce phase transformations in the SMAs. For excitation frequencies at which the displacements of the resonators are small, the beam response is not modified since the SMAs operate in the linear regime and no hysteretic damping is added to the structure.

#### IV. CONCLUSIONS

In this work, we explored locally resonant metamaterials that exploit shape memory alloy (SMA) springs in an effort to develop adaptive metamaterials that can exhibit tunable bandgap properties and also leverage amplitude dependent stress-induced phase transformations. An analytical model for a locally resonant metamaterial beam in transverse vibrations was combined with a shape memory spring model of the resonators to investigate and exploit the potential of temperature-induced phase transformations and stress-induced hysteretic behavior of the springs. Various case studies were presented for this new class of smart metamaterials and the resulting finite metastructures with specified boundary conditions.

It was shown that a metamaterial beam with SMA resonators can exhibit a tunable bandgap, since the natural frequency of the resonators (and hence the target frequency of the metamaterial) can be adjusted by properly changing the elastic modulus of the SMAs with temperature due to the reversible transition between the low-temperature martensitic phase and the high-temperature austenitic phase, which exhibit a lower elastic modulus and a larger elastic modulus, respectively. It was also shown that the SMA pseudoelastic hysteresis can improve the damping in the resulting frequency response functions substantially in order to create attenuation in the vibration modes outside the bandgap. This is particularly of interest for resonance frequencies that typically emerge right outside the bandgap in locally resonant metastructures. A significant decrease in the displacements of the resonator masses is also predicted for the pseudoelastic case.

Overall, the framework and results presented in this work can be used to design, analyze, and optimize tunable and potentially adaptive locally resonant metamaterials and metastructures leveraging SMAs. The one-dimensional concept given here for transverse vibrations of a classical beam can easily be extended to two-dimensional configurations as in the purely mechanical counterpart<sup>3</sup> of the problem.

#### ACKNOWLEDGMENTS

This work was supported by the São Paulo Research Foundation (FAPESP) [Grant Nos. 2017/08467-6 and 2015/26045-6] and by the Air Force Office of Scientific Research (AFOSR) Grant No. FA9550-15-1-0397.

<sup>1</sup>Z. Liu, X. Zhang, Y. Mao, Y. Y. Zhu, Z. Yang, C. T. Chan, and P. Sheng, *Science* **289**, 1734 (2000).

- <sup>2</sup>C. Sugino, S. Leadenham, M. Ruzzene, and A. Erturk, *J. Appl. Phys.* **120**, 134501 (2016).
- <sup>3</sup>C. Sugino, Y. Xia, S. Leadenham, M. Ruzzene, and A. Erturk, *J. Sound Vib.* **406**, 104 (2017).
- <sup>4</sup>K. M. Ho, C. K. Cheng, Z. Yang, X. X. Zhang, and P. Sheng, *Appl. Phys. Lett.* **83**, 5566 (2003).
- <sup>5</sup>F. Casadei, M. Ruzzene, L. Dozio, and K. A. Cunefare, *Smart Mater. Struct.* **19**, 015002 (2010).
- <sup>6</sup>Y. Jin, B. Bonello, and Y. Pan, *J. Phys. D: Appl. Phys.* **47**, 245301 (2014).
- <sup>7</sup>S. Chen, G. Wang, J. Wen, and X. Wen, *J. Sound Vib.* **332**, 1520 (2013).
- <sup>8</sup>Z. Yang, J. Mei, M. Yang, N. H. Chan, and P. Sheng, *Phys. Rev. Lett.* **101**, 204301 (2008).
- <sup>9</sup>M. Oudich, M. Senesi, M. B. Assouar, M. Ruzzene, J.-H. Sun, B. Vincent, Z. Hou, and T.-T. Wu, *Phys. Rev. B* **84**, 165136 (2011).
- <sup>10</sup>E. Baravelli and M. Ruzzene, *J. Sound Vib.* **332**, 6562 (2013).
- <sup>11</sup>R. Zhu, X. N. Liu, G. K. Hu, C. T. Sun, and G. L. Huang, *J. Sound Vib.* **333**, 2759 (2014).
- <sup>12</sup>K. H. Matlack, A. Bauhofer, S. Krödel, A. Palermo, and C. Daraio, *Proc. Natl. Acad. Sci.* **113**, 8386 (2016).
- <sup>13</sup>M. Nouh, O. Aldraihem, and A. Baz, *J. Sound Vib.* **341**, 53 (2015).
- <sup>14</sup>P. Wang, F. Casadei, S. Shan, J. C. Weaver, and K. Bertoldi, *Phys. Rev. Lett.* **113**, 014301 (2014).
- <sup>15</sup>Y. Xiao, J. Wen, and X. Wen, *J. Phys. D: Appl. Phys.* **45**, 195401 (2012).
- <sup>16</sup>H. Peng and P. F. Pai, *Int. J. Mech. Sci.* **89**, 350 (2014).
- <sup>17</sup>J. Li, X. Zhou, G. Huang, and G. Hu, *Smart Mater. Struct.* **25**, 045013 (2016).
- <sup>18</sup>C. Sugino, S. Leadenham, M. Ruzzene, and A. Erturk, *Smart Mater. Struct.* **26**, 055029 (2017).
- <sup>19</sup>G. Hu, L. Tang, A. Banerjee, and R. Das, *J. Vib. Acoust.* **139**, 011012 (2016).
- <sup>20</sup>G. Hu, L. Tang, and R. Das, *J. Appl. Phys.* **123**, 055107 (2018).
- <sup>21</sup>C. Xu, F. Cai, S. Xie, F. Li, R. Sun, X. Fu, R. Xiong, Y. Zhang, H. Zheng, and J. Li, *Phys. Rev. Appl.* **4**, 034009 (2015).
- <sup>22</sup>A. Casalotti, S. El-Borgi, and W. Lacarbonara, *Int. J. Non-Linear Mech.* **98**, 32 (2018).
- <sup>23</sup>L. Brinson, *J. Intell. Mater. Syst. Struct.* **4**, 229 (1993).
- <sup>24</sup>D. C. Lagoudas, *Shape Memory Alloys* (Springer US, Boston, MA, 2008), Vol. 1.
- <sup>25</sup>J. Frenzel, E. P. George, A. Dlouhy, C. Somsen, M. F. X. Wagner, and G. Eggeler, *Acta Mater.* **58**, 3444 (2010).
- <sup>26</sup>M. H. Elahinia, M. Hashemi, M. Tabesh, and S. B. Bhaduri, *Prog. Mater. Sci.* **57**, 911 (2012).
- <sup>27</sup>S. Saedi, A. S. Turabi, M. Taheri Andani, C. Haberland, H. Karaca, and M. Elahinia, *J. Alloys Compd.* **677**, 204 (2016).
- <sup>28</sup>M. G. Faulkner, J. J. Amalraj, and A. Bhattacharyya, *Smart Mater. Struct.* **9**, 632 (2000).
- <sup>29</sup>A. Bhattacharyya, L. Sweeney, and M. G. Faulkner, *Smart Mater. Struct.* **11**, 411 (2002).
- <sup>30</sup>R. N. Saunders, D. J. Hartl, J. G. Boyd, and D. C. Lagoudas, *Proc. SPIE* **9431**, 94310U (2015).
- <sup>31</sup>C. Liang and C. A. Rogers, *J. Intell. Mater. Syst. Struct.* **8**, 314 (1997).
- <sup>32</sup>F. S. Gandhi and D. Wolons, *Smart Mater. Struct.* **8**, 49 (1999).
- <sup>33</sup>J. Van Humbeeck, *J. Alloys Compd.* **355**, 58 (2003).
- <sup>34</sup>V. C. Sousa and C. De Marqui, Jr., *J. Intell. Mater. Syst. Struct.* **27**, 117 (2014).
- <sup>35</sup>V. C. Sousa and C. De Marqui, Jr., *J. Intell. Mater. Syst. Struct.* **29**, 623 (2018).
- <sup>36</sup>V. C. Sousa, C. De Marqui, Jr., and M. H. Elahinia, *Appl. Math. Modell.* **52**, 404 (2017).
- <sup>37</sup>F. Auricchio and E. Sacco, *Int. J. Solids Struct.* **38**, 6123 (2001).
- <sup>38</sup>R. Mirzaeifar, R. DesRoches, and A. Yavari, *Int. J. Solids Struct.* **48**, 611 (2011).
- <sup>39</sup>A. F. Saleeb, B. Dhakal, M. S. Hosseini, and S. A. Padula II, *Smart Mater. Struct.* **22**, 094006 (2013).
- <sup>40</sup>M. Frost, P. Sedlak, L. Kaderavek, L. Heller, and P. Sittner, *J. Intell. Mater. Syst. Struct.* **27**, 1927 (2015).
- <sup>41</sup>C. Cissé, W. Zaki, X. Gu, and T. Ben Zineb, *Mech. Mater.* **107**, 1 (2017).
- <sup>42</sup>C. Liang and C. Rogers, *J. Intell. Mater. Syst. Struct.* **1**, 207 (1990).
- <sup>43</sup>C. Liang and C. Rogers, *J. Eng. Math.* **26**, 429 (1992).
- <sup>44</sup>R. Mehrabi, M. Kadkhodaei, and M. H. Elahinia, *Smart Mater. Struct.* **23**, 075021 (2014).
- <sup>45</sup>S. Poorasadion, J. Arghavani, R. Naghdabadi, and S. Sohrabpour, *J. Intell. Mater. Syst. Struct.* **25**, 1905 (2014).
- <sup>46</sup>V. C. Sousa, C. De Marqui, Jr., and M. H. Elahinia, *J. Vib. Control* **24**, 1065 (2018).

- <sup>47</sup>F. Auricchio, D. Fugazza, and R. DesRoches, *J. Earthquake Eng.* **10**(supp001), 45 (2006).
- <sup>48</sup>O. E. Ozbulut, S. Hurlbaas, and R. DesRoches, *J. Intell. Mater. Syst. Struct.* **22**, 1531 (2011).
- <sup>49</sup>B. Huang, H. Zhang, H. Wang, and G. Song, *Smart Mater. Struct.* **23**, 065009 (2014).
- <sup>50</sup>S. Bhowmick and S. K. Mishra, *J. Intell. Mater. Syst. Struct.* **27**, 2062 (2016).
- <sup>51</sup>S. Sun and M. Lv, *J. Intell. Mater. Syst. Struct.* **27**, 1412 (2016).
- <sup>52</sup>R. A. A. Aguiar, M. A. Savi, and P. M. C. L. Pacheco, *J. Intell. Mater. Syst. Struct.* **24**, 247 (2012).
- <sup>53</sup>C.-Y. Lee and C.-A. Pai, *J. Intell. Mater. Syst. Struct.* **27**, 1047 (2016).
- <sup>54</sup>Y. Mani and M. Senthilkumar, *J. Vib. Control* **21**, 1838 (2015).
- <sup>55</sup>F. S. Gandhi and G. Chapuis, *J. Sound Vib.* **250**, 519 (2002).
- <sup>56</sup>F. Bachmann, R. Oliveira, A. Sigg, V. Schnyder, T. Delpero, R. Jaehne, A. Bergamini, V. Michaud, and P. Ermanni, *Smart Mater. Struct.* **21**, 075027 (2012).
- <sup>57</sup>M. M. Barzegari, M. Dardel, and A. Fathi, *J. Intell. Mater. Syst. Struct.* **26**, 988 (2015).
- <sup>58</sup>F. Auricchio, S. Morganti, A. Reali, and M. Urbano, *J. Mater. Eng. Perform.* **20**, 712 (2011).
- <sup>59</sup>R. Razavilar, A. Fathi, M. Dardel, and J. Arghavani Hadi, *Proc. Inst. Mech. Eng., Part K: J. Multi-body Dyn.* **232**, 253 (2018).
- <sup>60</sup>R. Razavilar, A. Fathi, M. Dardel, and J. Arghavani Hadi, *J. Intell. Mater. Syst. Struct.* **29**, 1835 (2018).
- <sup>61</sup>L. Meirovitch, *Principles and Techniques of Vibration* (Prentice Hall, Upper Saddle River, NJ, 1997), p. 694.